

**First principles modeling of CO<sub>2</sub> adsorption on (100), (010), and (001) surfaces  
of wollastonite for applications in enhanced rock weathering**

Brian Luan<sup>1</sup> and Pratik P. Dholabhai<sup>2\*</sup>

*<sup>1</sup>School of Chemistry and Materials Science  
Rochester Institute of Technology  
Rochester, NY 14623*

*<sup>2</sup>School of Physics and Astronomy  
Rochester Institute of Technology  
Rochester, NY 14623*

\* Email: [pratik.dholabhai@rit.edu](mailto:pratik.dholabhai@rit.edu)

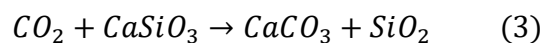
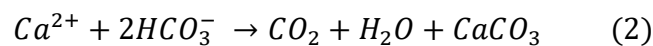
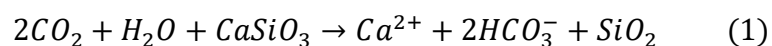
## Abstract

Negative emissions technologies target the removal of carbon dioxide (CO<sub>2</sub>) from the atmosphere as a way of combating global warming. Enhanced rock weathering (ERW) is a vital negative emissions technology that applied globally could remove gigatonnes of CO<sub>2</sub> per year from the atmosphere. In ERW, silicate minerals exposed to the atmosphere trap CO<sub>2</sub> via mineral carbonation as thermodynamically stable carbonates. To obtain an atomic scale understanding of the weathering process and to design more reactive silicates for enhanced rock weathering, CO<sub>2</sub> adsorption on low index wollastonite (CaSiO<sub>3</sub>) surfaces was modeled using density functional theory. Atomic scale structure of (100), (010), and (001) surfaces of wollastonite was predicted and the thermodynamics of their interaction with CO<sub>2</sub> was modeled. Based on surface energy calculations, (001) and (010) surfaces of wollastonite exhibit similar stabilities, while (100) surface is found to be least stable. Depending on the surface structure and chemistry, different CO<sub>2</sub> adsorption geometries are possible. A common trend emerges, wherein CO<sub>2</sub> adsorbs molecularly and demonstrates proclivity to bond with surface layer calcium and oxygen binding sites. Mechanisms for electronic charge transfer between the adsorbate and the substrate were studied to shed light on the fundamental aspects of these interactions. The most favorable bent CO<sub>2</sub> geometry was bridged between calcium atoms, revealing that the enhancing the likelihood of this geometry and binding site could pave the way to designing reactive silicates for efficient CO<sub>2</sub> sequestration via ERW.

**Keywords:** CO<sub>2</sub> sequestration, enhanced rock weathering, density functional theory, electronic structure, silicate minerals

## 1. Introduction

Atmospheric concentrations of greenhouse gases such as carbon dioxide (CO<sub>2</sub>) have increased due to the burning of fossil fuels, which contributes to a rise in global temperatures, ocean acidification, and climate change.<sup>1</sup> There is a global commitment to reducing carbon emissions as seen in the United Nations Framework Convention on Climate Change Paris Agreement (UNFCCC) signed by many nations around the world.<sup>2</sup> One strategy put forth to decrease the emissions is through enhanced rock weathering (ERW).<sup>3</sup> ERW is one negative emissions technology that could remove gigatonnes of CO<sub>2</sub> per year from the atmosphere.<sup>4,5,6</sup> This technique involves the chemical weathering of silicate rocks by CO<sub>2</sub> to form carbonates. In ERW, CO<sub>2</sub> sequestration occurs via spreading of silicate minerals on croplands and in the ocean where exposure to the atmosphere, soil porewater, and oceanic waters causes CO<sub>2</sub> to be trapped via thermodynamically stable carbonates.<sup>4,5</sup> This spreading of crushed minerals enhances the amount and speed of CO<sub>2</sub> sequestered by natural rock weathering by introducing more reactive minerals for weathering to act on. Silicates are chosen as the mineral for carbon sequestration because they are abundant and the mechanism for weathering is spontaneous.<sup>7</sup> **Equation 1** shows the weathering process of calcium silicates, and **Equation 2** shows the formation of carbonates as a result of the weathering process. This formation is carried out by marine animals making shells or by precipitation of carbonates out of water into solid rock. The overall sequestration in **Equation 3** shows that for every formula unit of silicate weathered, one molecule of carbon dioxide is captured.



Croplands augmented by silicates for ERW have been shown to sequester carbon and boost plant growth.<sup>8</sup> The present challenge facing ERW irrespective of method is cost and availability of materials.<sup>9</sup> From a fundamental and technological standpoint, the present challenge is that the most reactive naturally-occurring silicates such as wollastonite are not

abundant.<sup>10</sup> In order to design novel synthetic silicates for ERW, a basic understanding of their structure and reactivity is necessitated at the atomic scale and nanoscale. Designing novel synthetic silicates requires an understanding of their structure and reactivity at an atomic level to overcome these challenges.<sup>11</sup>

Atomistic simulations such as force field molecular dynamics and density functional theory (DFT) have been used to successfully determine the surface structure of silicates and their interaction with molecules.<sup>11,12,13,14</sup> Water activation of carbonation along with differences between the water-free and water-assisted reaction pathways have been investigated.<sup>15</sup> Nonetheless, these computational studies are still in their infancy, resulting in a lack of clarity regarding the atomic scale structure of low-index silicate surfaces and basic atomistic mechanisms and dynamics of CO<sub>2</sub> interaction with various facets of silicates. For instance, although much is known about the surface structure and properties of well-studied complex materials such as titanium dioxide, cerium oxide, strontium titanate, *etc.*, the same cannot be argued about wollastonite or silicates in general.<sup>16,17,18</sup> Moreover, several of wollastonite low-index surfaces are Type II asymmetric according to Tasker classification, which requires careful treatment for ensuring appropriate surface cleavage so as to avoid surface energy divergence.<sup>19</sup> The same is true for other silicates surfaces since the inherent complexity is common across various silicates, which requires careful examination from a theoretical and computational perspective.

Wollastonite (CaSiO<sub>3</sub>) is a silicate mineral formed by chains of silicon-oxygen tetrahedrons coordinated by calcium.<sup>20</sup> The unit cell contains two apex-to-apex joining tetrahedra and the tetrahedron with one edge parallel to the chain direction in the *b*-axis. Wollastonite most commonly crystallizes into the triclinic system with space group P1 ( $\alpha$ -wollastonite). Carbonation of wollastonite is known to occur spontaneously, which can be thought to occur through an acid base reaction between carbonic acid and a rock base. Reportedly, carbonic acid is formed *in situ* between water, carbon dioxide and a calcium ion.<sup>7</sup>

Herein, we report first principles DFT calculations to predict the atomic scale structure and stability of (100), (010), and (001) surfaces of wollastonite. We further examine the thermodynamics of CO<sub>2</sub> adsorption on these surfaces. The fundamental interaction of these adsorbed species with surfaces is studied in detail. We further shed light on the electronic structure of the surface and surface-adsorbate systems as well as the electronic charge transfer

after the adsorption of CO<sub>2</sub>. Notably, results herein shed light on the importance of understanding the intricate interaction between CO<sub>2</sub> and low-index surfaces of wollastonite for ERW applications. Atomic scale studies of ERW predicts that carbon dioxide preferentially adsorbs at oxygen and calcium sites forming calcium carbonate precursors. Overall, these results offer atomic scale insights pertaining to the thermodynamic preferences of CO<sub>2</sub> capture by silicate surfaces.

## 2. Computational Method

Electronic structure calculations were performed using density functional theory (DFT) implemented in the *Vienna ab initio Simulation Package* (VASP).<sup>21, 22, 23, 24</sup> Spin polarized calculations were performed using the Perdew-Burke-Ernzerhof (PBE) functional<sup>25</sup> within the generalized gradient approximation (GGA).<sup>26, 27</sup> Kohn-Sham equations were solved using a plane wave basis set with a projected augmented wave (PAW) method that replicates the effect of core electrons on valence electrons.<sup>28, 29</sup> To ensure accurate results, a plane-wave cutoff energy of 400 eV was utilized, which converged the energies to approximately 0.01 meV. Integration of the first Brillouin-zone was performed using Monkhorst–Pack *k*-point mesh with a Gaussian smearing of 0.1 eV.<sup>30</sup> A  $10 \times 10 \times 10$  and  $2 \times 2 \times 1$  mesh was used to relax the bulk and the surface structure, respectively. Using a conjugate gradient algorithm, ground state geometries of different systems were obtained by minimizing the Hellman–Feynman forces until the total forces on each atom were less than 0.01 eV/Å.<sup>31, 32</sup>

Wollastonite in its most common triclinic phase crystallizes in space group P1 with the experimental lattice constants  $a = 7.94$  Å,  $b = 7.32$  Å, and  $c = 7.07$  Å with six formula units per unit cell.<sup>33</sup> Supercells were constructed from layers of wollastonite with three-dimensional periodic boundary conditions. No evidence of surface reconstructions has been reported in experiments. As a result, we model the wollastonite surfaces with optimized truncated bulk surfaces, which is similar to approach in literature studies.<sup>11, 12, 13</sup> Supercells for (100), (010), and (001) surface slabs contained 240 atoms (48 calcium, 48 silicon and 144 oxygen) with  $2 \times 2 \times 2$  periodicity built from the 30-atom wollastonite unit cell. We have used 4 layers of CaSiO<sub>3</sub>, with 60 atoms in each layer ( $2 \times 2$ ) for a total of 240-atom supercell. To mimic the surface, a vacuum of 15 Å was added along the *z*-axis (normal to the surface). Essentially, for all the slab models, the two surfaces are separated by roughly 15 Å, ensuring that the interaction between the two surface layers is minimal. We have not conducted convergence tests for thickness of surface

slabs since we have utilized sufficiently large slabs and a 15 Å vacuum layer. As compared to literature work on  $\alpha$ -wollastonite surfaces,<sup>11</sup> the surface slabs used in this work are almost twice in thickness. As a result, we have reasonable confidence that the surface models used herein offer enough fidelity to perform adsorption calculations. Importantly, in the present 240-atom supercell, adsorbed CO<sub>2</sub> molecule is separated from its periodic image by ~30 Å, which is very reasonable to avoid any potential interaction amid periodic CO<sub>2</sub> molecules. In the present calculations, we have not explicitly considered dispersion interactions, which might alter some quantitative data pertaining to stability of CO<sub>2</sub> molecule. However, we expect that the qualitative understanding of the adsorption process offered in this work would not be strongly influenced by the exclusion of dispersion corrections, which commonly lead to a scaled shift in predicted energies. All the constructed models are stoichiometric, and the two resulting surfaces in the slab due to periodic boundary conditions have the same initial atomic structure, prior to further optimization. Parameters for convergence of plane waves and atomic positions were chosen based on previous values that converged for similar system.<sup>14</sup> Electronic and Structural Analysis (VESTA) package for was utilized for the visualization of electronic and charge density structures.<sup>34,35</sup>

### 3. Results and Discussion

#### 3.1 Surface stability

Geometrically and energetically minimized atomic scale models of (001), (010), and (100) surfaces of wollastonite are given in **Figure 1**, which were constructed using the optimized bulk structure. Owing to the triclinic phase, wollastonite exhibits different and complex surface layer atomic arrangement and symmetry along (100), (010), and (001) surfaces. The normal (**Figure 1a, 1b, 1c**) and side (**Figure 1d, 1e, 1f**) views of the surface atomic arrangement in wollastonite evidently display the complexity associated with studying such systems. Remarkably, in each of the three surface models, atomic layers could either constitute calcium, oxygen, or silicon or a combination of these atoms, which further dictate the surface stability. Surface energy for wollastonite surfaces was calculated using **Equation 4**,

$$\gamma = \frac{1}{2A}(E_{surface} - nE_{bulk}) \quad (4)$$

where  $E_{surface}$  is the total energy of the surface slab structure and  $E_{bulk}$  is the total energy of the bulk structure. The factor of  $n$  is used to ensure the energies of surface slab and bulk structures contain the same number of atoms – here  $n = 8$ . Additionally,  $A$  is the surface area, and the factor of two is included because there are two surfaces in the model. The surface energies calculated were 1.349 J/m<sup>2</sup>, 1.103 J/m<sup>2</sup>, and 1.104 J/m<sup>2</sup> for the (100), (010), and (001) respectively. Clearly, the (010) and (001) surfaces are the most stable with almost similar stabilities, whereas (100) is found to be least stable. In the case of (100) surface, the surface layer primarily comprises calcium and oxygen atoms. On the other hand, the surface layer in (010) and (001) surfaces contain calcium, silicon, and oxygen atoms, which primarily explain their slightly different surface stabilities. For the (001) surface, these results are in reasonable agreement with the surface energy of 1.028 J/m<sup>2</sup> reported by Sanna *et al.*, who utilized DFT with the PW91 functional.<sup>14</sup> In addition, Kundu *et al.* reported a value of 1.36 J/m<sup>2</sup> for (001) obtained using force fields.<sup>12,13</sup> Overall, the computed (001) surface energy value is in reasonable agreement with literature value, and since (100) and (010) surfaces were built and minimized using similar methodology, it provides enough confidence that the surface models predicted in this work are accurate. Importantly, they offer a good starting point to study CO<sub>2</sub> adsorption on wollastonite (100), (010), and (001) surfaces.

From the calculated surface energies of the (100), (010), and (001) surfaces, the equilibrium crystal morphology (**Figure 2**) was constructed using the Wulff's method,<sup>36</sup> which correlates the surface energies to the morphology of the wollastonite nanocrystal. It is imperative to note that for the present case, the equilibrium morphology has been obtained using only three minimum energy surfaces. As a result, it is likely that the true equilibrium morphology might slightly differ than that presented herein since the stability of other low index surfaces could potentially alter the predicted morphology. However, a vital aspect evident from the Wulff construction given in **Figure 2** is that all three surfaces are exposed in the wollastonite nanocrystal.

**Figure 1.** For geometrically optimized surface slabs, normal (top) views of (100), (010), and (001) surfaces are given in (a), (b), and (c) respectively. Side views of these surfaces are given in

(d), (e), and (f). Visible in the normal view are possible adsorption sites for CO<sub>2</sub>. Side view displays the intricate stacking of atomic planes along with the silicate chains in the [010] direction characteristic of the wollastonite crystal. Gold, blue, and red spheres represent calcium, silicon, and oxygen atoms, respectively.

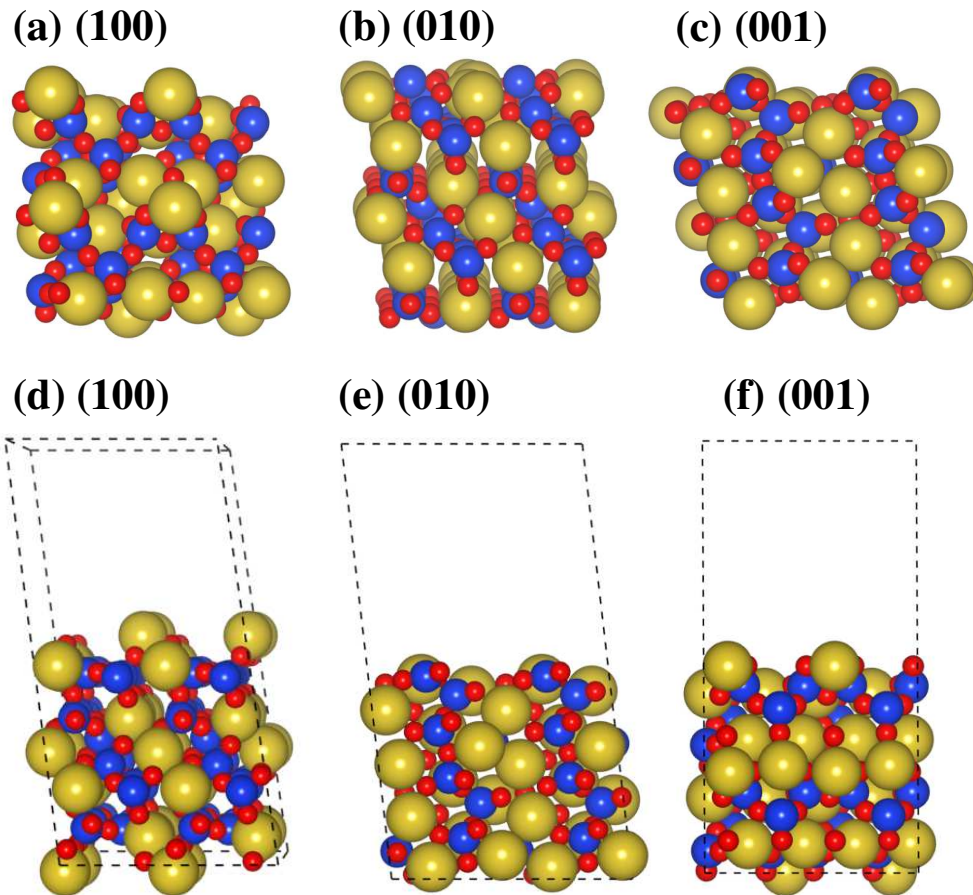
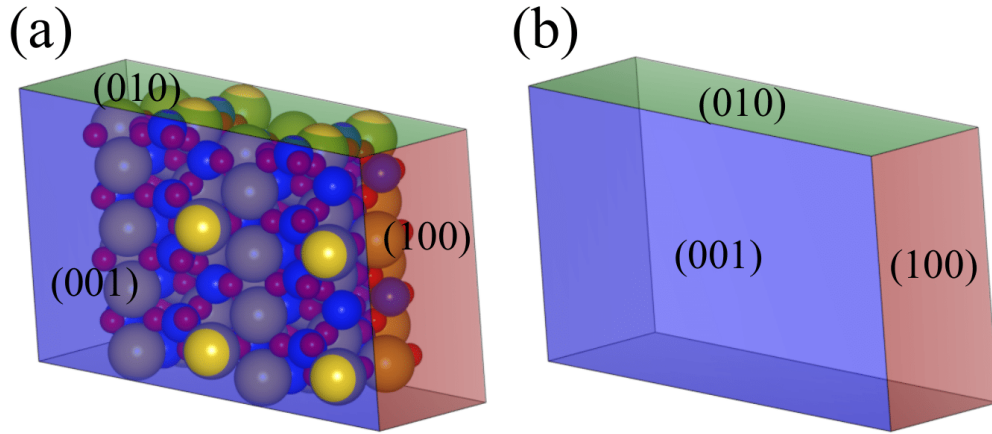


**Figure 2.** Wulff shape of wollastonite constructed from the (100), (010) and (001) surfaces as seen in (a) and (b). The Wulff shape with atoms can be seen in (a), whereas that with just the Wulff shape is given in (b).





### 3.2 Adsorption of CO<sub>2</sub> and surface charge transfer

To comprehend the atomic scale interaction and adsorption mechanism of CO<sub>2</sub> on wollastonite surfaces, a single CO<sub>2</sub> molecule was adsorbed onto low index (100), (010), and (001) surfaces of clean wollastonite. The adsorption energy ( $E_{ads}$ ) of CO<sub>2</sub> was calculated using **Equation 5**,

$$E_{ads} = E_{surf+CO_2} - E_{surf} - E_{CO_2} \quad (5)$$

wherein  $E_{surf+CO_2}$  is the energy of the surface slab containing the CO<sub>2</sub> molecule,  $E_{surf}$  is the energy of the clean slab, and  $E_{CO_2}$  is the energy of the gas phase CO<sub>2</sub> molecule. The isolated gas phase CO<sub>2</sub> molecule was modelled in a vacuum at the center of the same supercell used for surfaces, as well as keeping the same accuracy parameters described for the surfaces. There are three atomic surface sites, namely calcium, silicon, and oxygen that are probable candidates for adsorption – depending on the surface geometries, CO<sub>2</sub> can be adsorbed directly onto the top site or bridging sites in the neighborhood of these atoms. Adsorption energies for various minimized geometries of CO<sub>2</sub> molecule adsorbed on wollastonite are given in **Table 1**. A normal view of adsorption sites in the supercells is depicted in **Figure 3** for (100), (010), and (001) surfaces. In addition, adsorption sites along with the final geometry of the CO<sub>2</sub> molecule are also offered in **Table 1** with corresponding geometries given in **Figure 3**. Distinct adsorption sites were chosen

to ensure that they are not repeated due to symmetric sites along the  $2 \times 2$  periodicity of the supercells shown in **Figure 3**.

**Figure 3.** Possible surface sites for CO<sub>2</sub> adsorption on (a) (100), (b) (010), and (c) (001) surfaces of wollastonite. Corresponding details of the atomic geometry of CO<sub>2</sub> and respective surface layer adsorption sites are explained in **Table 1**. Atomic color scheme is same as in **Figure 1**.

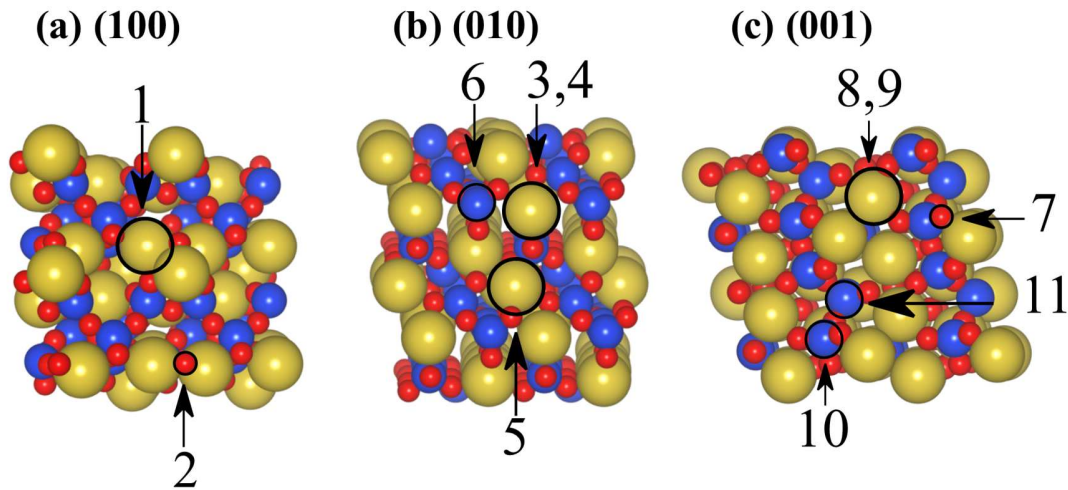


**Table 1.** Adsorption energies (eV) of CO<sub>2</sub> on different adsorption sites for the three surfaces considered. Adsorption energies were calculated using **Equation 5**. Site number corresponds to the adsorption sites given in **Figure 3**. Parallel ( $\parallel$ ) and perpendicular ( $\perp$ ) symbols refer to CO<sub>2</sub> orientation relative to the surface. The angle ( $\angle$ ) symbol denotes a 45° angle with respect to the surface. D, B, and L refer to dissociative, bent, and linear geometries of CO<sub>2</sub>, respectively.

Surface	Site number	Binding site and CO <sub>2</sub> geometry	Adsorption energy (eV)
(100)	1	Ca, $\parallel$ , D	5.08
(100)	2	O, $\parallel$ , B	-2.45
(010)	3	Ca, $\perp$ , L	-0.23

(010)	4	Ca,   , L	-0.18
(010)	5	Ca, ∠, L	-0.16
(010)	6	Si, ⊥, L	-0.12
(001)	7	O,   , B	-0.44
(001)	8	Ca, ∠, L	-0.51
(001)	9	Ca, ⊥, L	-0.42
(001)	10	Si,   , L	-0.34
(001)	11	Si, ⊥, L	0.54

As evident in **Table 1**, calcium and oxygen sites are thermodynamically preferred for CO<sub>2</sub> adsorption compared to silicon sites since their adsorption energies are lower for the same surfaces considered. Moreover, for some silicon adsorption sites, we were not able to identify a stable minimized geometry, indicating that adsorption of CO<sub>2</sub> at silicon sites is less likely. As explained in **Table 1**, one dissociative adsorption geometry of CO<sub>2</sub> is possible. In addition, two molecular geometries of CO<sub>2</sub> that are likely to occur after adsorption are linear and bent. In general, linear molecular CO<sub>2</sub> configurations are more common as this is the most stable molecular form in gas phase. In the linear configurations, one of the end oxygen atoms of CO<sub>2</sub> is primarily adsorbed onto the surface, whereas the central carbon atom does not directly participate in the adsorption process. Bond lengths between the carbon and oxygen in the linear CO<sub>2</sub> molecule are between ~1.15-1.20 Å, comparable to the equilibrium bond length. In contrast, bent CO<sub>2</sub> molecule observed at **Sites 2** and **7** have the central carbon adsorb onto a surface oxygen ion. In this case, both the oxygen atoms of the adsorbed CO<sub>2</sub> interact with nearby surface calcium ions. C – O bond length in the CO<sub>2</sub> molecule elongate to ~1.25-1.30 Å, which would be expected in a carbonate ion. The bond lengths between the carbon atom and surface oxygen ion are in the range of ~1.3-1.5 Å, which reveal that there is a stronger interaction between the carbon and oxygens in the CO<sub>2</sub> molecule than that observed between carbon and surface oxygen ion in the wollastonite surface. There is another less probable adsorption geometry, wherein the CO<sub>2</sub> molecule dissociates into a CO molecule and an O atom. In this observed dissociative adsorption at **Site 1**, the CO molecule is adsorbed onto a surface calcium ion whereas the O atom moved into a pocket under the calcium ion. **Site 1** is found to be the least favorable geometry

with a very high adsorption energy, indicating that adsorption of CO<sub>2</sub> at **Site 1** is extremely unlikely to occur. To focus on likely scenarios for CO<sub>2</sub> adsorption that are thermodynamically favorable, we restrict our focus to molecular CO<sub>2</sub> adsorption in linear and bent geometries.

Optimized geometries of four favorable adsorption sites are shown in **Figure 4** and **Figure 5**. The lowest energy structure, **Site 2**, adopts a geometry wherein the CO<sub>2</sub> molecule forms a bent conformation on the (100) surface as shown in **Figure 4a**. **Site 7** also converges to a similar bent conformation on the (001) surface (**Figure 5a**). In these bent geometries, adsorption of the CO<sub>2</sub> molecule onto a surface oxygen formed a trigonal planar carbonate ion, which further stabilizes the overall structure. In **Site 2** (**Figure 4a**), the trigonal planar structure is bridged between two calcium atoms and the two bent oxygens of the CO<sub>2</sub>. The CO<sub>2</sub> molecule in **Site 7** (**Figure 5a**) is also adsorbed onto a surface oxygen. However, in this case, it only interacts with one calcium ion rendering it less stable than **Site 2**. In **Site 2**, a pocket forms from surface reconstruction that fits the carbonate, wherein one of the bridging surface calcium ions breaks periodicity and moved 0.9 Å towards the adsorbed CO<sub>2</sub>. The surface region around this pocket experiences noticeable reconstruction leading to the shifting of SiO<sub>4</sub> tetrahedrons to accommodate the movement of the larger calcium ion. The most pronounced surface reconstruction observed among all the adsorption sites is in **Site 2**. On the contrary, **Site 7** experienced much less surface reconstruction because CO<sub>2</sub> interacts primarily with only one nearby calcium ion. In this case, the bridge position between two calcium ions is not formed, since the next closest calcium ion is ~2.0 Å apart, which makes it energetically less favorable to relax. Overall, due to the resulting bridge position, **Site 2** has an adsorption energy of -2.45 eV as compared to **Site 7**, which has an adsorption energy of -0.44 eV.

To obtain a fundamental understanding of charge transfer upon adsorption and elucidate the interaction between wollastonite surfaces and CO<sub>2</sub>, electronic charge densities before and after the adsorption process were computed for all the cases considered. Charge density difference ( $\Delta\rho$ ) structures were computed using **Equation 6**,

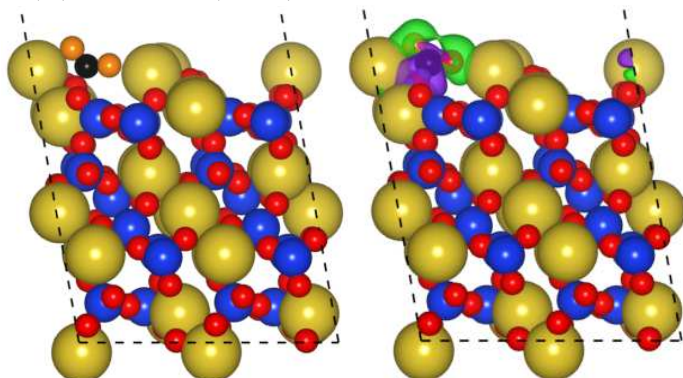
$$\Delta\rho = \rho_{CO_2/Surface} - \rho_{Surface} - \rho_{CO_2} \quad (6)$$

wherein  $\rho_{CO_2/Surface}$  correspond to the charge density of the adsorbed (final) system, whereas  $\rho_{Surface}$  and  $\rho_{CO_2}$  correspond to the charge density of clean wollastonite surface and isolated

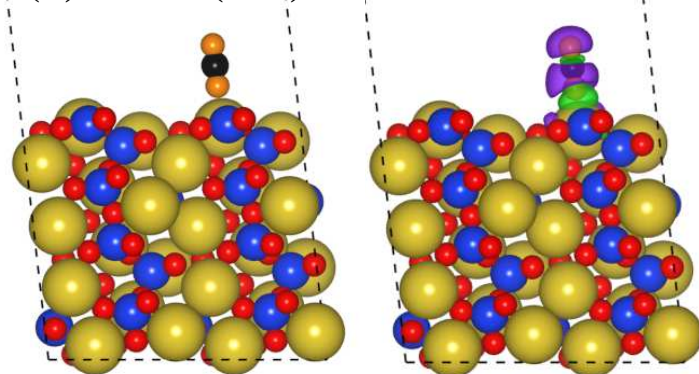
CO<sub>2</sub> molecule, respectively. The charge density of the isolated CO<sub>2</sub> molecule was taken to have the same geometry and relative positions as the adsorbed molecule for the respective site. Hence,  $\Delta\rho$  demonstrates the charge density variations in wollastonite and CO<sub>2</sub> when they are brought in contact. As shown in the electron density difference plot for **Site 2** (**Figure 4a**), loss of electron density in the region of the carbon adsorption to the surface oxygen is observed, whereas the oxygens in the CO<sub>2</sub> gain electron density. Loss of electron density at the adsorption site and gain of electron density in the region of the bent oxygens in CO<sub>2</sub> reveal the stronger interaction with the surface in that region. This charge transfer process offers evidence that the CO<sub>2</sub> molecule causes the surface reconstruction partly due to its proclivity to bond with the surface calcium ion and form the carbonate. **Site 7** exhibits a similar difference charge density plot with a net loss of electron density in the vicinity of the carbon atom as well as the adsorption site. This is compensated by the bent oxygens of the CO<sub>2</sub> molecule, which display an increase in their electron density. However, dissimilar to **Site 2**, only one of the oxygens in CO<sub>2</sub> interacts with calcium ion. An increase of electron density on one of the oxygens in CO<sub>2</sub> from being in the bent configuration without another calcium to stabilize the increase could potentially explain why **Site 7** is higher in energy as compared to **Site 2**.

**Figure 4.** Side views of favorable adsorption and electron density difference plots for (a) Site 2 on (100) surface and (b) Site 3 on (010) surface. Atomic color scheme for wollastonite is same as in **Figure 1**. For CO<sub>2</sub> molecule, orange and black correspond to oxygen and carbon atoms, respectively. In the difference charge density plots, green denotes regions of electron density accumulation and purple indicates regions of electron density depletion.

**(a) Site 2 (100)**



**(b) Site 3 (010)**



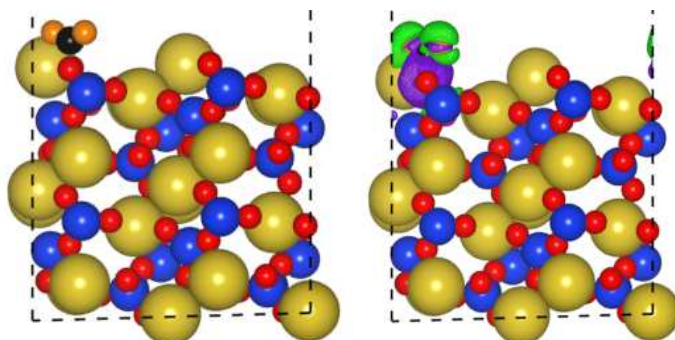
The stable bent geometries of **Site 2** and **Site 7** can be contrasted with less stable linear CO<sub>2</sub> geometries at **Site 3** (**Figure 4b**) on (010) surface and **Site 8** (**Figure 5b**) on (001) surface. Linear geometries of CO<sub>2</sub> adsorb to the surface through one of the oxygen atoms. For instance, at **Site 3**, the linear CO<sub>2</sub> is adsorbed perpendicular to the surface directly onto a calcium ion. Charge density difference plot for this configuration elucidates the interaction between CO<sub>2</sub> and surface calcium atom. At the interface between the oxygen and wollastonite surface, there is an increase of electron density. The surface lost electron density to oxygen atom in CO<sub>2</sub> except for the bond between the carbon and surface nonbonded oxygen which gained electron density. This configuration has an adsorption energy of -0.23 eV, which is still favorable but higher in energy as compared to other sites for CO<sub>2</sub> adsorption. This can be explained by closely looking at the structure, which shows that only the initially adsorbed oxygen is close enough to the surface to interact with it creating little orbital overlap to minimize energy. Virtually no surface

reconstruction is observed for this adsorption site reinforcing the idea that CO<sub>2</sub> only interacts with the calcium ion.

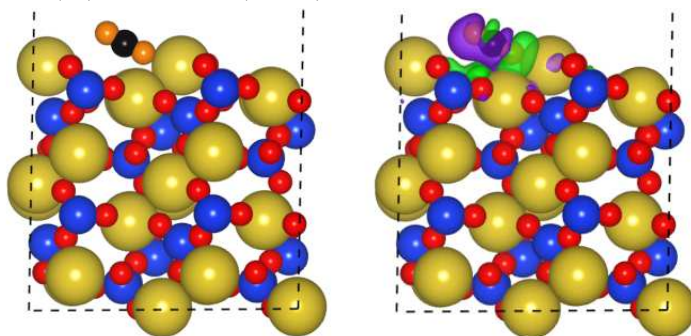
Analogous to **Site 3**, at **Site 8 (Figure 4b)**, CO<sub>2</sub> exhibits a thermodynamic preference to adsorb with a linear geometry. **Site 8** has an adsorption energy of -0.51 eV, which is lower as compared to **Site 3**. At **Site 8**, the linear CO<sub>2</sub> molecule was adsorbed to the side of a calcium atom, but at an angle of ~45°, which is in contrast with the perpendicular orientation observed at **Site 3**. Evident from the charge density difference plot in **Figure 5b**, similar features for the electronic charge density difference that emerged at **Site 3** are also observed at **Site 8**. At the interface of CO<sub>2</sub> oxygen and surface calcium, there was an increase of electron density. However, the wollastonite surface and CO<sub>2</sub> lost some electronic charge density except for the bond between the carbon and surface nonbonded oxygen. The tilted geometry relative to the surface allowed for greater orbital overlap between CO<sub>2</sub> and the surface atoms further stabilizing the configuration. This is apparent in the electron density difference plot in **Figure 5b**, wherein significant electron density increase is observed between the tilted CO<sub>2</sub> particle and the surface atoms it is floating above. Some surface reconstruction in this neighborhood gives further evidence that the tilted CO<sub>2</sub> is stabilized by its interactions with the surface. Essentially, the four difference charge density plots given in **Figure 4** and **5** capture the common features encountered across the various adsorption sites studied in this work. For brevity, we have not included analysis for additional adsorption sites.

**Figure 5.** Side views of favorable adsorption and electron density difference plots for (a) Site 7 on (001) surface and (b) Site 8 on (001) surface. Atomic color scheme is same as in **Figure 3**. In the difference charge density plots, green denotes regions of electron density accumulation and purple indicates regions of electron density depletion.

**(a) Site 7 (001)**



**(b) Site 8 (001)**



Since the DFT calculations were performed at 0 K, the bent as well as linear CO<sub>2</sub> geometries are likely to occur directly depending on the surface adsorption site. For the bent CO<sub>2</sub> geometries, since adsorption process at both **Site 2** and **Site 7** (**Table 1**) is exothermic, presence of transition states or barriers for the observed bending of CO<sub>2</sub> are less likely. In general, bent geometry at **Site 2** is the most favorable. As a result, under ambient conditions, we would expect that CO<sub>2</sub> capture is more probable in the bent configuration as compared to the linear configuration. Although the prediction of vibrational modes of adsorbed CO<sub>2</sub> would be valuable in assignment of binding modes, we have not computed them in this work due to very high computational cost involved. These calculations are planned for future work. Experimental results for various geometries of CO<sub>2</sub> adsorbed on wollastonite are not available in the literature since most experiments are focused on investigating the full carbonation process leading to calcium carbonate. However, future experiments targeting CO<sub>2</sub> adsorption on wollastonite



surfaces would further reinforce the theoretical results pertaining to thermodynamics of CO<sub>2</sub> adsorption.

### 3.3 Electronic structure analysis

Detailed density of states (DOS) analysis was performed to gain insights into the electronic structure of the wollastonite surface before and after the adsorption of CO<sub>2</sub>. By comparing the DOS before and after CO<sub>2</sub> adsorption, modifications in the electronic states can be visualized near the Fermi level and a fundamental understanding of CO<sub>2</sub> interaction with wollastonite surfaces can be obtained. DOS plots in **Figure 6**, **7**, and **8** show the number of available states for electrons to occupy at different energy levels. In all the DOS plots, the Fermi level has been shifted to 0 eV – this level is at the top of the valence band because DFT calculations take place at 0 K. As a result, low lying and valence band states are filled while conductance band states above the Fermi level are empty (virtual). **Figure 6** shows the DOS of clean (001) surface of wollastonite. Evidently, the energy levels at top of the valence band are predominantly occupied by O 2*p* with some Ca 3*d* and Si 3*s* states. However, As seen in **Figure 6a**, silicon states are less prominent in low-lying, valence, and conductance states as compared to oxygen and calcium. In order to focus on the features around the Fermi level, **Figure 6b** offers a magnified plot for **Figure 6a**. Lower amounts of silicon states explain why CO<sub>2</sub> does not prefer to adsorb at silicon sites – there are less sites available at the surface to participate in bonding with CO<sub>2</sub>. On the other hand, oxygen and calcium states are prominent in both the valence and the conductance bands, indicating their accessibility to participate in bonding with CO<sub>2</sub>. DOS for (100) and (010) are not shown since they are qualitatively and quantitatively almost similar to that of (001) surface. For (100), (010), and (001) surfaces of wollastonite, the calculated band gaps are 2.69 eV, 3.02 eV and 3.12 eV, respectively. DFT typically underestimates the bandgaps, which appears to be the case for  $\alpha$ -wollastonite since experiments report a band gap of 4.18 eV.<sup>37</sup>

**Figure 6. (a)** Electronic density of states (DOS) projected onto Ca, Si, and O atoms of the (001) wollastonite surface. **(b)** Magnified region near the Fermi level is shown, and low-lying states are neglected. Only spin-up channel is shown. In all cases, the Fermi energy level is shifted to 0 eV.

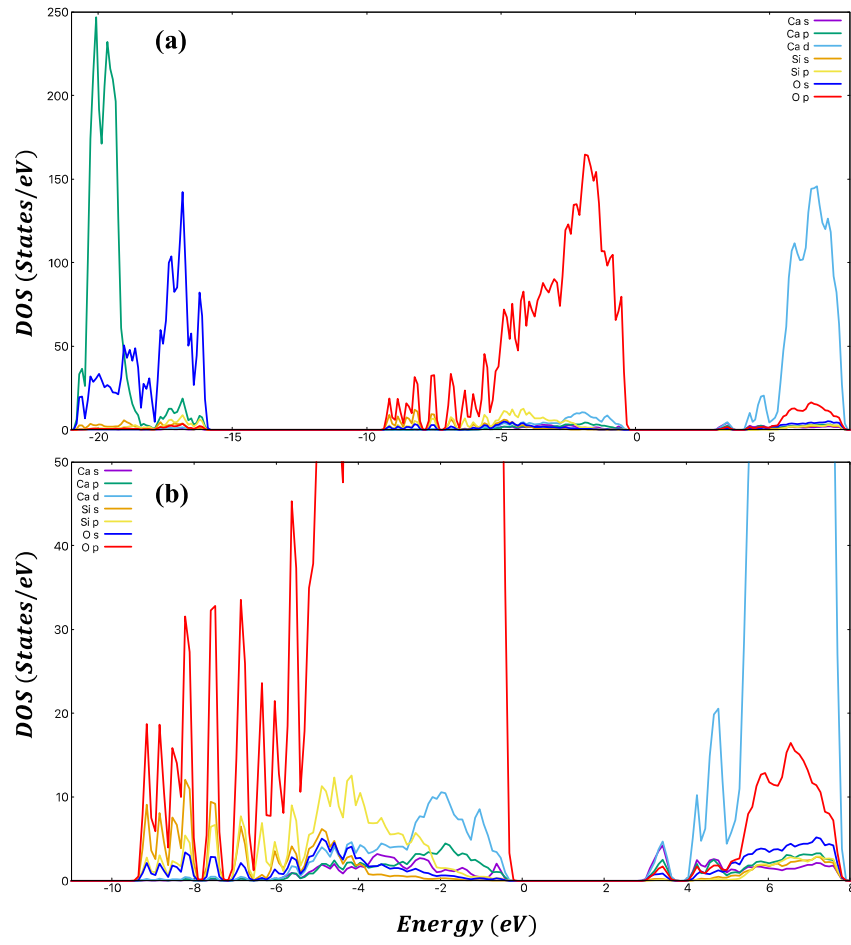
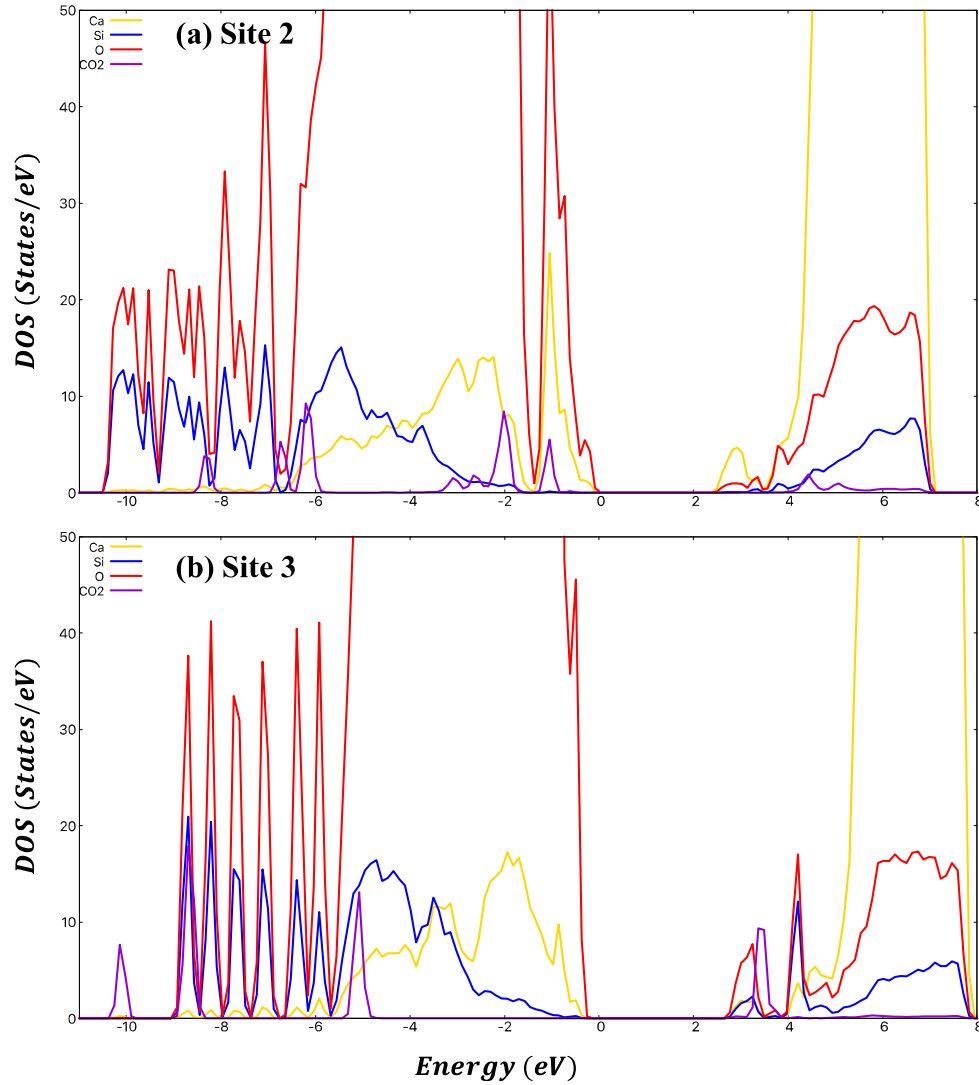


**Figure 7.** (a) DOS projected onto Ca, Si, and O atoms of the (100) wollastonite surface and CO<sub>2</sub> molecule adsorbed on Site 2. (b) DOS projected onto Ca, Si, and O atoms of the (010) wollastonite surface and CO<sub>2</sub> molecule adsorbed on Site 3. Only the magnified region near the Fermi level is shown. Only spin-up channel is shown. In all cases, the Fermi energy level is shifted to 0 eV.

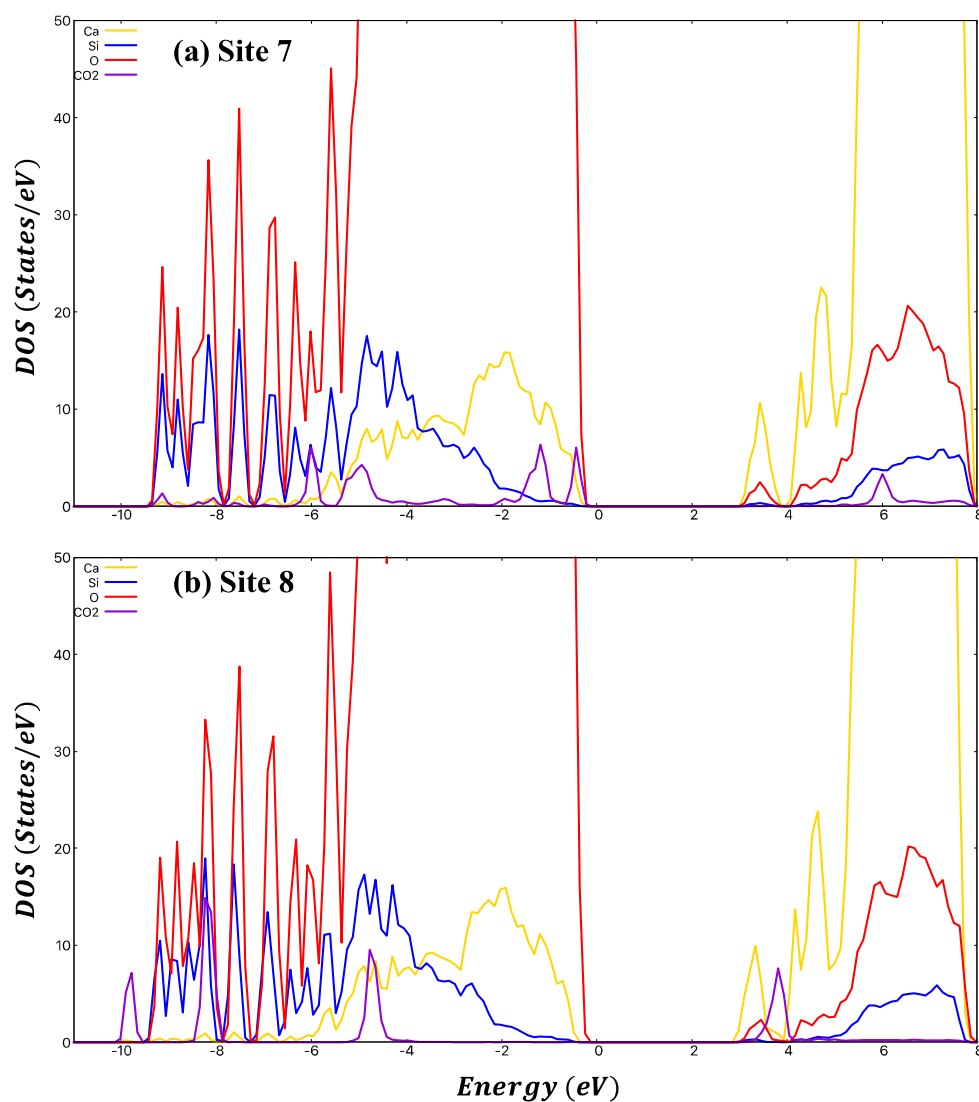


It is important to note that the qualitative features of DOS for various configurations with linear CO<sub>2</sub> are similar. Likewise, qualitative features of DOS for the two bent CO<sub>2</sub> geometries are alike. As a result, to offer a concise discussion of DOS analysis of adsorbed configurations, we focus on precisely the same four adsorption sites that were discussed using difference charge density. **Figure 7** shows DOS plots for adsorption **Site 2** on (100) surface and **Site 3** on (010) surface. In addition, **Figure 8** shows DOS plots for adsorption **Site 7** and **8**, both on (001) surface. All the DOS plots have been shown for the same magnified region of **Figure 6b**. As compared to the clean wollastonite surfaces, adsorption sites on (100), (010), and (001) surfaces have the overall DOS of the Ca, Si and O atoms slightly shifted. As shown in **Figure 7** and **8**,

there is a distinct difference in CO<sub>2</sub> states between the bent and the straight geometries of CO<sub>2</sub>. Both the linear geometries of **Site 3 (Figure 7b)** and **Site 8 (Figure 8b)** have three peaks in the valence band around -10.0, -8.0 and -4.8 eV with another peak below 4.0 eV in the conductance band. The bent CO<sub>2</sub> geometries lead to CO<sub>2</sub> peaks shifting upwards in energy to better overlap surface states as seen in **Site 2 (Figure 7a)** and **Site 7 (Figure 8a)**. Both the bent geometries have two peaks in the range -2.0 – 0.0 eV at the edge of the valence band. **Site 2** has additional peaks at -8.5, -6.5 and -6.0 eV, whereas **Site 7** has two additional peaks at around -6.0 and -5.0 eV. Changes in CO<sub>2</sub> geometry result in modifications in orbital structure which is visible in the DOS. Linear geometries display peaks lower in the valence band, which have less overlap with the O 2*p* and Ca 3*d* states as wollastonite surface states are greater in the vicinity of the valence band edge. Bent CO<sub>2</sub> is more conducive for adsorption because the change in geometry shifts its peaks closer to the valence band, which has better overlap with the wollastonite surface states. Linear CO<sub>2</sub> has states that are lower in energy in the valence band, and as a result, they do not overlap considerably with wollastonite surface states.

Both the electron charge density difference analysis and DOS analysis support bent CO<sub>2</sub> adsorption geometries being more stable as compared to the linear CO<sub>2</sub> geometries. Charge density difference structures show that in the bent geometries, CO<sub>2</sub> gains electron density on oxygen atoms. Electronic density gains are more stable when they interact with surface calcium atoms in a bridge position. As shown in **Figure 7a**, there is a large Ca 3*d* and O 2*p* peak present around -1.0 eV for **Site 2** that is not present in either the other surfaces or other adsorption sites. This peak has distinctly separated itself from the rest of the valence band states and overlaps a CO<sub>2</sub> peak in the same region – this overlap of states at the edge of the valence band are expected to stabilize the structure. Analogous to **Site 2**, the bent CO<sub>2</sub> structure seen in **Site 7** also occurred for adsorption onto a surface oxygen atom but had a higher adsorption energy of -0.44 eV compared to adsorption onto calcium atoms on the same (001) surface. Although this configuration had a bent CO<sub>2</sub> geometry, owing to the atomic positions of the surface calcium atoms, a bridge position for the CO<sub>2</sub> to absorb was not able to form. **Site 7 (Figure 8a)** did not consist a peak separating from the rest of the valence band. From these fundamental insights, we conclude that a combination of the bent CO<sub>2</sub> geometry and wollastonite surface reconstruction that facilitates a bridge position is responsible for the most thermodynamically stable adsorption configuration.

**Figure 8.** DOS projected onto Ca, Si, and O atoms of the (001) wollastonite surface and CO<sub>2</sub> molecule adsorbed on **(a) Site 7** and **(b) Site 8**. Only the magnified region near the Fermi level is shown. Only spin-up channel is shown. In all cases, the Fermi energy level is shifted to 0 eV.



On the contrary, linear CO<sub>2</sub> adsorption geometries uncovered at **Site 3** and **Site 8** are not able to form the aforementioned bridge position between two calcium ions. In this scenario, the

Ca  $3d$  states that are needed to overlap with the states in the  $\text{CO}_2$  to form the bridge position are most prominent between  $-3.0 - -1.0$  eV; the  $\text{CO}_2$  valence band peak in linear geometries is at around  $-4.0$  eV, which is bit too far away from the calcium states for strong adsorption. Atomic scale structure of wollastonite surfaces impacts this modification in  $\text{CO}_2$  geometry by rendering some adsorption sites more favorable than the others via creation of bent  $\text{CO}_2$  geometries. Surface calcium ions with corresponding  $\text{SiO}_4$  tetrahedra geometry close to oxygen adsorption sites allows for the creation of the bridge structure for  $\text{CO}_2$  adsorption. Bent  $\text{CO}_2$  adsorption onto a surface oxygen ion produces a trigonal planar geometry of the carbonate that would be the product of weathering. Increasing the number of bent  $\text{CO}_2$  adsorption sites could enhance the weathering rate of wollastonite and other similar silicate minerals.

Fundamental insights pertaining to the atomic scale interaction of  $\text{CO}_2$  with wollastonite offered in this work will be instrumental for designing the next-generation synthetic silicates for  $\text{CO}_2$  sequestration via ERW. Silicates being one of the most abundant materials on earth span a variety of different applications and synthesis methods. Some common synthesis methods include chemical precipitation, solid state sintering, and sol-gel prior to calcination.<sup>38,39,40</sup> These techniques offer potential through additional reactions and doping to produce tunable and sustainable materials for weathering. Insights from the adsorption of  $\text{CO}_2$  could be potentially used to guide synthesis of novel silicates. Although we have strictly focused on the thermodynamics of  $\text{CO}_2$  adsorption, future studies targeting the kinetics of adsorption process would further assist with the design of novel silicates for ERW. It has been previously shown that the presence of water influences the carbonation of wollastonite through a metal-proton exchange.<sup>11,38</sup> Carbonation of wollastonite stops after a localized surface monolayer has been produced for the cases of water-free and hydrated surfaces. However, in the case of heavily hydrated surface, calcium ions are partially removed from solid phase into the water/wollastonite interface allowing for delocalized carbonates to be formed. Nitrogen and oxygen at ambient conditions could also stabilize  $\text{CO}_2$  through dispersion interactions or compete for binding sites which is unknown. It is imperative to note that although the current work studies the adsorption of a single  $\text{CO}_2$  molecule, increasing the coverage of  $\text{CO}_2$  would assist in understanding coverage dependent adsorption. Even though understanding the intricate role of water (**Equation 1**) in ERW is beyond the scope of the current work, future atomistic studies focused on elucidating the role of water and other atmospheric species in influencing  $\text{CO}_2$  adsorption would

offer further details about the reactivity of silicate surfaces and their future synthesis for ERW. Low reactivity of silicon adsorption sites opens the possibility of doping silicon to enhance the reactivity of silicates and comprehend the role of dopants and defects in enhancing the reactivity of silicates for ERW.

#### **4. Conclusions**

Carbon dioxide adsorption onto wollastonite silicates for enhanced rock weathering is thermodynamically favorable. Adsorption of bent  $\text{CO}_2$  geometries on oxygen sites of wollastonite surfaces are most energetically stable and are needed for the eventual production of carbonate. Density of states reveal that the bent geometries of  $\text{CO}_2$  bring electron states closer to the edge of the valence band where they can overlap better with an increased amount of wollastonite surface calcium and oxygen states. Silicon adsorption sites on wollastonite surfaces are not as favorable as surface calcium and oxygen sites. Consequently, silicon could be a prime target for doping to increase the surface reactivity or otherwise modify the surface structure for enhanced  $\text{CO}_2$  adsorption. Surface layer chemistry of wollastonite play a vital role in influencing the formation of bent  $\text{CO}_2$  geometries because without the two bridging calcium atoms at the surface that stabilize the bent structure, adsorption energies of linear  $\text{CO}_2$  geometries would be comparable to bent geometries. In general, fundamental insights of the adsorption mechanisms of  $\text{CO}_2$  on (100), (010), and (001) surfaces of wollastonite are offered, which is expected to assist with the design and synthesis of next-generation silicates for enhanced rock weathering.

#### **Conflicts of interest**

There are no conflicts to declare.

#### **Acknowledgments**

This work is supported by the Alfred P. Sloan Foundation Grant Number 2021-14167. PPD acknowledges fruitful discussions with Andrea Hicks and Rafael M. Santos as well as discussions at the Negative Emissions Science Scialog hosted by the Research Corporation for Science Advancement. This work used computational resources provided by the Extreme Science and Engineering Discovery Environment (XSEDE), which is supported by the National

Science Foundation (NSF) grant number ACI-1548562. The authors also acknowledge partial computing resources from Research Computing at Rochester Institute of Technology.

## References

---

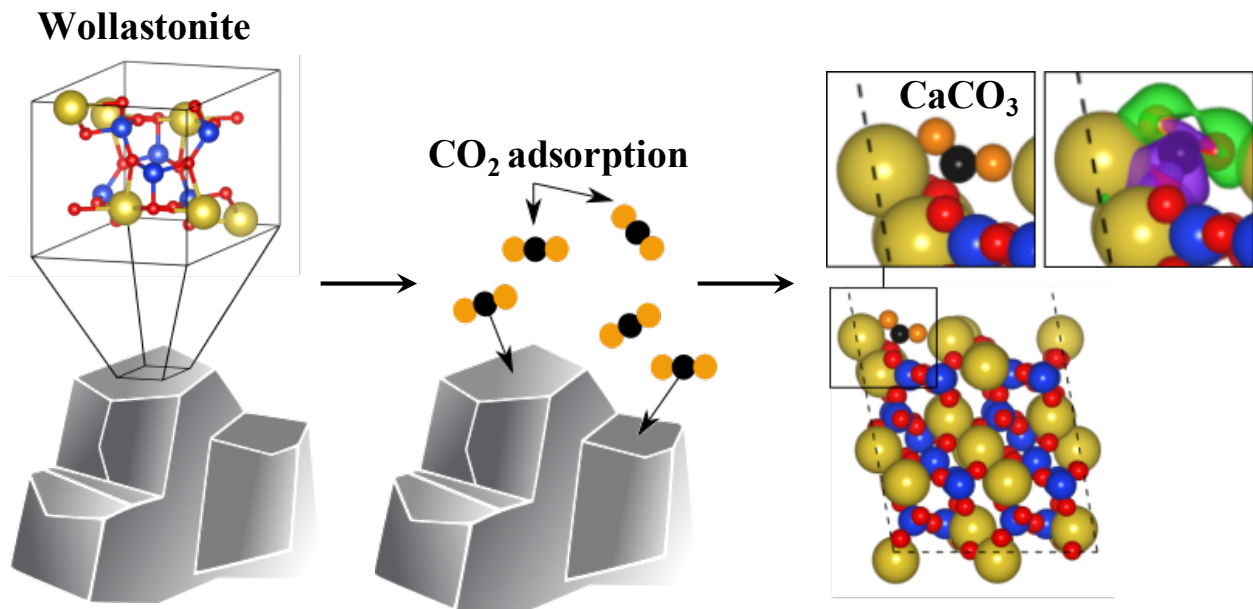
- <sup>1</sup> S. Arrhenius, On the Influence of Carbonic Acid in the Air upon the Temperature of the Ground, *Philosophical Magazine and Journal of Science Series 5*, 41 (1896) 237-276
- <sup>2</sup> Intergovernmental Panel on Climate Change, *Climate Change 2021 - The Physical Science Basis*.  
<https://www.ipcc.ch/report/sixth-assessment-report-working-group-i/>
- <sup>3</sup> M. Pilch, CO<sub>2</sub> Disposal by Means of Silicates. *Nature*, 345 (1990) 486.
- <sup>4</sup> K. Lackner, A Guide to CO<sub>2</sub> Sequestration. *Science*, 300 (2003) 1677-1678.  
<https://www.science.org/doi/10.1126/science.1079033>
- <sup>5</sup> D. Beerling, E. Kantzas, M. Lomas, P. Wade, R. Eufrasio, P. Renforth, B. Sarkar, M. Andrews, R. James, C. R. Pearce, J. F. Mercure, H. Pollitt, P. B. Holden, N. R. Edwards, M. Khanna, L. Koh, S. Quegan, N. F. Pidgeon, I. A. Janssens, J. Hansen and S. A. Banwart, Potential for Large-scale CO<sub>2</sub> Removal Via Enhanced Rock Weathering with Croplands. *Nature*, 583 (2020) 242–248.  
<https://doi.org/10.1038/s41586-020-2448-9>.
- <sup>6</sup> F. Haque, R. M. Santos and Y. Chiang, Urban Farming with Enhanced Rock Weathering as a Prospective Climate Stabilization Wedge. *Environmental Science & Technology*, 55 (2021) 13575–13578. <https://doi.org/10.1021/acs.est.1c04111>
- <sup>7</sup> J. C. S. Wu, J. D. Sheen, S. Y. Chen and Y. C. Fan, Feasibility of CO<sub>2</sub> Fixation via Artificial Rock Weathering. *Ind. Eng. Chem. Res.*, 40(18) (2001) 3902–3905.  
<https://doi.org/10.1021/ie010222l>.
- <sup>8</sup> F. Haque, R. M. Santos, A. Dutta, M. Thimmanagari and Y. W. Chiang, Co-Benefits of Wollastonite Weathering in Agriculture: CO<sub>2</sub> Sequestration and Promoted Plant Growth. *ACS Omega*, 4(1) (2019) 1425–1433. <https://doi.org/10.1021/acsomega.8b02477>.
- <sup>9</sup> P. Renforth, C.-L. Washbourne, J. Taylder and D. A. C. Manning, Silicate Production and Availability for Mineral Carbonation. *Environ. Sci. Technol.*, 45 (6) (2011) 2035–2041.  
<https://doi.org/10.1021/es103241w>.



- 
- <sup>10</sup> A. Brioché, Mineral Commodity Summaries – Wollastonite. *United States Geological Survey*, 2020
- <sup>11</sup> R. C. Longo, K. Cho, P. Brünner, A. Welle, A. Gerdes and P. Thissen, Carbonation of Wollastonite (001) Competing Hydration: Microscopic Insights from Ion Spectroscopy and Density Functional Theory. *ACS Appl. Mater. Interfaces*, 7(8) (2015) 4706–4712.  
<https://doi.org/10.1021/am508313g>.
- <sup>12</sup> T. K. Kundu, K. Hanumantha Rao and S. C. Parker, Atomistic Simulation of the Surface Structure of Wollastonite and Adsorption Phenomena Relevant to Flotation. *Int. J. Miner. Process.*, 72 (1-4) (2003) 111–127. [https://doi.org/10.1016/S0301-7516\(03\)00092-9](https://doi.org/10.1016/S0301-7516(03)00092-9)
- <sup>13</sup> T. K. Kundu, K. Hanumantha Rao and S. C. Parker, Atomistic Simulation of the Surface Structure of Wollastonite. *Chem. Phys. Lett.*, 377(1-2) (2003) 81–92.  
[https://doi.org/10.1016/S0009-2614\(03\)01097-2](https://doi.org/10.1016/S0009-2614(03)01097-2).
- <sup>14</sup> S. Sanna, W. G. Schmidt and P. Thissen, Formation of Hydroxyl Groups at Calcium-Silicate Hydrate (C-S-H): Coexistence of Ca–OH and Si–OH on Wollastonite (001). *J. Phys. Chem. C*, 118 (15) (2014) 8007–8013. <https://doi.org/10.1021/jp500170t>.
- <sup>15</sup> K. Garbev, P. Stemmermann, L. Black, C. Breen, J. Yarwood and B. Gasharova, Structural Features of C-S-H(I) and Its Carbonation in Air? A Raman Spectroscopic Study. Part I: Fresh Phases. *J. Am. Ceram. Soc.*, 90 (3) (2007) 900–907.  
<https://doi.org/10.1111/j.1551-2916.2006.01428.x>.
- <sup>16</sup> U. Diebold, The Surface Science of Titanium Dioxide. *Surf. Sci. Rep.*, 48 (5-8) (2003) 53–229.  
[https://doi.org/10.1016/S0167-5729\(02\)00100-0](https://doi.org/10.1016/S0167-5729(02)00100-0).
- <sup>17</sup> D. R. Mullins, The Surface Chemistry of Cerium Oxide. *Surf. Sci. Rep.*, 70 (1) (2015) 42–85.  
<https://doi.org/10.1016/j.surfrep.2014.12.001>.
- <sup>18</sup> B. L. Phoon, C. W. Lai, J. C. Juan, P. Show and W. Chen, A Review of Synthesis and Morphology of SrTiO<sub>3</sub> for Energy and Other Applications. *Int. J. Energy Res.*, 43 (10) (2019) 5151–5174. <https://doi.org/10.1002/er.4505>.
- <sup>19</sup> P. W. Tasker, The Stability of Ionic Crystal Surfaces. *J. Phys. C Solid State Phys.*, 12 (22) (1979) 4977–4984. <https://doi.org/10.1088/0022-3719/12/22/036>.
- <sup>20</sup> Y. Ohashi, Polysynthetically-Twinned Structures of Enstatite and Wollastonite. *Phys. Chem. Miner.*, 10 (5) (1984) 217–229. <https://doi.org/10.1007/BF00309314>.

- 
- <sup>21</sup> G. Kresse and J. Furthmüller, Efficiency of Ab-Initio Total Energy Calculations for Metals and Semiconductors Using a Plane-Wave Basis Set. *Comput. Mater. Sci.*, 6 (1) (1996) 15–50. [https://doi.org/10.1016/0927-0256\(96\)00008-0](https://doi.org/10.1016/0927-0256(96)00008-0)
- <sup>22</sup> G. Kresse and J. Furthmüller, Efficient Iterative Schemes for Ab Initio Total-Energy Calculations Using a Plane-Wave Basis Set. *Phys. Rev. B*, 54 (16) (1996) 11169–11186. <https://doi.org/10.1103/PhysRevB.54.11169>
- <sup>23</sup> G. Kresse and J. Hafner, Ab Initio Molecular Dynamics for Liquid Metals. *Phys. Rev. B*, 47 (1) (1993) 558–561. <https://doi.org/10.1103/PhysRevB.47.558>
- <sup>24</sup> G. Kresse and J. Hafner, Ab Initio Molecular-Dynamics Simulation of the Liquid-Metal--Amorphous-Semiconductor Transition in Germanium. *Phys. Rev. B*, 49 (20) (1994) 14251–14269. <https://doi.org/10.1103/PhysRevB.49.14251>
- <sup>25</sup> J. P. Perdew, K. Burke and M. Ernzerhof, Generalized Gradient Approximation Made Simple. *Phys. Rev. Lett.*, 77 (18) 1996 3865–3868. <https://doi.org/10.1103/PhysRevLett.77.3865>.
- <sup>26</sup> P. Hohenberg and W. Kohn, Inhomogeneous Electron Gas. *Phys. Rev.*, 136 (1964) B864. <https://doi.org/10.1103/PhysRev.136.B864>
- <sup>27</sup> W. Kohn and L.J. Sham, Self-Consistent Equations Including Exchange and Correlation Effects. *Phys. Rev.*, 140 (1965) A1133. <https://doi.org/10.1103/PhysRev.140.A1133>
- <sup>28</sup> P.E. Blöchl, Projector Augmented-Wave Method. *Phys. Rev. B*, 50 (24) (1994) 17953–17979. <https://doi.org/10.1103/PhysRevB.50.17953>.
- <sup>29</sup> G. Kresse and D. Joubert, From Ultrasoft Pseudopotentials to the Projector Augmented-Wave Method. *Phys. Rev. B*, 59 (3) (1999) 1758–1775. <https://doi.org/10.1103/PhysRevB.59.1758>.
- <sup>30</sup> H. J. Monkhorst and J. D. Pack, Special Points for Brillouin-Zone Integrations. *Phys. Rev. B*, 13 (12) (1976) 5188–5192. <https://doi.org/10.1103/PhysRevB.13.5188>.
- <sup>31</sup> H. Hellman, *Introduction to Quantum Chemistry*; Deuticke, Leipzig, 1937.
- <sup>32</sup> R. P. Feynman, Forces in Molecules. *Phys. Rev.*, 56 (4) (1939) 340–343. <https://doi.org/10.1103/PhysRev.56.340>.
- <sup>33</sup> S. Milani, D. Comboni, P. Lotti, P. Fumagalli, L. Ziberna, J. Maurice, M. Hanfland and M. Merlini, Crystal Structure Evolution of CaSiO<sub>3</sub> Polymorphs at Earth's Mantle Pressures. *Minerals*, 11 (2021) 652. <https://doi.org/10.3390/min11060652>

- 
- <sup>34</sup> K. Momma and F. Izumi, *VESTA: A Three-Dimensional Visualization System for Electronic and Structural Analysis. J. Appl. Crystallogr.*, 41 (3) (2008) 653–658.  
<https://doi.org/10.1107/S0021889808012016>.
- <sup>35</sup> K. Momma and F. Izumi, *VESTA 3 for Three-Dimensional Visualization of Crystal, Volumetric and Morphology Data. J. Appl. Crystallogr.*, 44 (6) (2011) 1272–1276.  
<https://doi.org/10.1107/S0021889811038970>.
- <sup>36</sup> G. Wulff, *Z. Krist.* 34, (1901) 449. <https://doi.org/10.1524/zkri.1901.34.1.449>
- <sup>37</sup> K. A. Almasri, H. A. A. Sidek, K. A. Matori, and M. H. M. Zaid, Effect of Sintering Temperature on Physical, Structural and Optical Properties of Wollastonite Based Glass-Ceramic Derived from Waste Soda Lime Silica Glasses. *Results Phys.* 7, (2017) 2242.  
<https://doi.org/10.1016/j.rinp.2017.04.022>
- <sup>38</sup> R. C. Longo, R. Königer, A. Nefedov, and P. Thissen, Chemical Properties of Metal-Silicates Rendered by Metal Exchange Reaction. *ACS Sustain. Chem. Eng.* 7, (2019) 8449.  
<https://doi.org/10.1021/acssuschemeng.9b00157>
- <sup>39</sup> R. C. Longo, N. Schewe, P. G. Weidler, S. Heissler, and P. Thissen, Synthesis of Silicates for High-Performance Oxide Semiconductors: Electronic Structure Analysis. *ACS Appl. Electron. Mater.* 3, (2021) 299. <https://doi.org/10.1021/acsaelm.0c00856>
- <sup>40</sup> Y. J. No, J. J. Li, and H. Zreiqat, Doped Calcium Silicate Ceramics: A New Class of Candidates for Synthetic Bone Substitutes. *Materials*, 10, (2017) 153.  
<https://doi.org/10.3390/ma10020153>



**Enhanced rock weathering of wollastonite for CO<sub>2</sub> sequestration**